A New Fourth-Order Processing Algorithm for Spaceborne SAR

KNUT ELDHUSET
Norwegian Defence Research Establishment

A new fourth-order signal aperture radar (SAR) processing algorithm has been developed for a general satellite-Earth relative motion. The two-dimensional exact transfer function (ETF) is calculated and range-variant phase corrections have been calculated in order to process many azimuth lines per block. The ETF together with the phase corrections has been called the fourth-order EETF (extended ETF). It is also shown that a fourth-order EETF is necessary to process high quality images from spaceborne SAR with long integration times with spatial resolution around 1 m. The algorithm is fast and is anticipated to have good phase preservation properties.

Manuscript received September 7, 1995; revised October 22, 1996 and September 20, 1997.

IEEE Log No. T-AES/34/3/06016.

This work was supported by the Norwegian Defence Research Establishment.

Author's address: Norwegian Defence Research Establishment, Division for Electronics, P.O. Box 25, N-2007 Kjeller, Norway.

I. INTRODUCTION

A. Background

Several synthetic aperture radar (SAR) processing algorithms have been developed since the first spaceborne SAR (SEASAT) was launched in 1978. The range-Doppler algorithm [1] was the first fast algorithm used for processing spaceborne SAR data but was later refined to accommodate secondary range compression [2]. This algorithm is still used for processing SAR data operationally. Since about 1987 more advanced algorithms have also appeared which take care of the phase quality in the processed signal data. The ω-k algorithm, which was borrowed from seismics, was introduced in [3 and 4]. This algorithm was based on the wave equation and inspired development of another phase preserving algorithm [5]. In [5] they invoked SAR-specific considerations in order to improve the processing efficiency and ease of implementation. However, the latest algorithm, the chirp scaling (CS) approach [6–8] has nearly perfected the airborne SAR processing. No interpolation is needed in this algorithm. Another approach for fast processing has been analyzed in [9]. All the mentioned algorithms were derived based on the airborne SAR geometry.

The airborne SAR algorithms referred to above have been adapted for spaceborne SAR processing by calculating a squint angle which is dependent on the Doppler frequency caused by Earth rotation. To take into account the orbital motion of the satellite a scaled satellite speed (effective velocity) is used for estimation of the azimuth Doppler rate. For small azimuth beam angles a straight line motion with an effective velocity (radar velocity) may be a good approximation to a circular motion of a spaceborne SAR, but not to a general relative motion between a satellite and the rotating Earth. A general second-order relative motion was first treated in [10] in order to use state vectors of the satellite directly. In this approach two parameters, the Doppler centroid and the azimuth Doppler rate, could be used to describe the relative motion. Hence, the azimuth phase history was expressed by these two parameters, which again are functions of the state vectors of the satellite and the rotation of the Earth. This formalism was used in [11] in the expression given for the second-order two-dimensional exact transfer function (ETF) for a spaceborne SAR. The work described in [11] uses the "spaceborne SAR" formalism and not the "airborne SAR" formalism. The ETF algorithm treats a general waveform of transmitted signal while the original CS algorithm assumes a linear FM chirp in the transmitted signal.

All the mentioned algorithms were derived based on second-order azimuth phase history. An ETF algorithm was calculated exactly in [12] for simulation

of an airborne spotSAR in a circular trajectory and in [13] for a wide-beam spaceborne SAR for a perfectly circular orbit around a planet. In the last case the rotation of the planet was not included.

B. Objectives

With all the above algorithms above in mind we do a further development in processing of spaceborne SAR data. We have in mind possible future SAR systems with long integration times, such as wide azimuth beam SAR, look steering SAR or spotSAR. In all the algorithms mentioned in Section IA apart from [12, 13] the azimuth phase history is described by two parameters, the Doppler centroid and the azimuth Doppler rate (or alternatively an effective radar velocity). We use the formalism established in [10, 11] and the second-order azimuth phase history development in [10] is extended to fourth-order. New formulas for the fourth-order ETF are calculated. The ETF performs the bulk of the SAR compression and would be exact if the Doppler parameters were range invariant. To cope with varying Doppler parameters in the cross-track direction and to increase the speed of the ETF, new formulas for range-variant phase corrections are developed. In this way many azimuth lines can be processed with the same ETF. In this work the limitation of block size in range is determined for a specific case. The azimuth variation of Doppler parameters is not treated here since the range variation is the main problem. However, it can in principle be included in the algorithm. The ETF algorithm with phase corrections is referred to as the fourth-order extended ETF algorithm (fourth-order EETF or EETF4). A second-order EETF with simpler expressions than for the fourth-order EETF has been developed by the author and is applicable for ERS-1, ERS-2, RADARSAT, and ENVISAT [14]. The EETF described here doesn't perform curvature equalization as in [8], however, this is not very important for a spaceborne SAR since the variation of the range curvature over a swath is much smaller than for airborne SAR.

In Section IIA a fourth-order azimuth phase history model is established and in Section IIB it is shown how the parameters of this model can be estimated. In Section III the fourth-order EETF algorithm is described. Section IIIA shows the general Fourier transform calculation of the point target response and Section IIIB shows the fourth-order case. Range-variant fourth-order phase corrections are calculated in Section IIIC. The implementation of the algorithm is briefly described in Section IIID. In Section IV raw data of point targets are simulated to test the algorithm. In Section IVA some examples are selected to demonstrate that second-order azimuth phase history is not sufficient with long integration times and in Section IVB some simulated point target responses processed with the 2D EETF4 are shown and their quality are assessed.

II. AZIMUTH PHASE HISTORY MODEL

In most publications (e.g. [1, 4, 8, 9]) the phase history is developed based on airborne SAR geometry where the aircraft moves in a straight line. For spaceborne SARs the aircraft geometry is modified as explained in Section IA by incorporating an effective squint angle and an effective satellite velocity (e.g. [15]). The phase history is not expanded around the beam center, but about the time of closest approach which may be far from the beam center. An expansion about the beam center with zero time [5, 10] is a more natural way to proceed for very high Doppler centroids, especially if the time of integration is long (e.g. when 1 m azimuth resolution is required). The formalism introduced in [10] and later used in [16] will now be extended to 4th order.

A. Fourth-Order Taylor Expansion

One can approximate the relative satellite-Earth motion using a fourth-order Taylor expansion in azimuth time (slow time) t_a

$$\vec{R}(t_a) \cong \vec{R} + t_a\vec{V} + \tfrac{1}{2}t_a^2\vec{A} + \tfrac{1}{6}t_a^3\vec{B} + \tfrac{1}{24}t_a^4\vec{C} \qquad (1)$$

where $\vec{R}$, $\vec{V}$, $\vec{A}$, $\vec{B}$, $\vec{C}$ are 3-dimensional relative position, velocity, acceleration, rate of acceleration, and rate of the rate of acceleration vectors between the satellite and a given target on the earth at azimuth time 0. Equation (1) is a 3-dimensional vector equation and the azimuth time is associated with the motion of the satellite in the azimuth direction. The geometry is simply illustrated in Fig. 1. The position vector of the satellite (S) and the position vector of the target (T) are denoted $\vec{R}_S$ and $\vec{R}_T$, respectively. For simplicity, the velocity vector of the satellite, $\vec{V}_S$, is defined as the azimuth direction and is coincident with the y-axis of the attitude reference system in Fig. 1. This is generally not the case. The axes of the attitude reference system which is fixed to the satellite is denoted with three vectors $\vec{X}_A$, $\vec{Y}_A$, and $\vec{Z}_A$. Usually the attitude control system tries to make the z-axis ($\vec{Z}_A$) perpendicular to the surface of the Earth. The look angle a for a given target in the range direction is indicated in the figure. All vectors are defined in an inertial system with axes denoted X_I, Y_I, and Z_I with the origin at the geocenter. The different vectors in (1) (at zero azimuth time) are given by

$$\vec{R} = \vec{R}_S - \vec{R}_T \qquad (2)$$

$$\vec{V} = \vec{V}_S - \vec{V}_T \qquad (3)$$

$$\vec{A} = \vec{A}_S - \vec{A}_T \qquad (4)$$

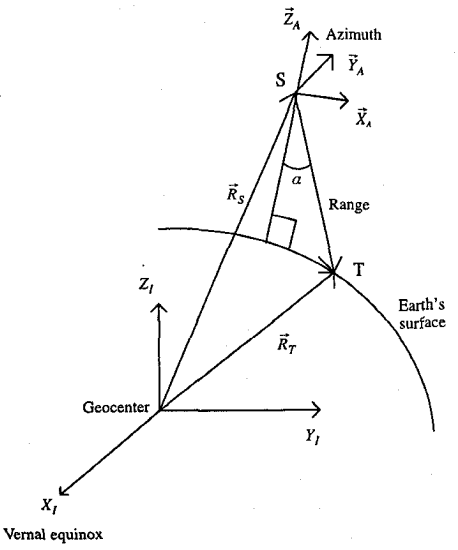

Fig. 1. Relative satellite-Earth motion in inertial reference frame (X_I,Y_I,Z_I). Attitude reference frame fixed to satellite (S) also shown.

$$\vec{B} = \vec{B}_S - \vec{B}_T \tag{5}$$

$$\vec{C} = \vec{C}_S - \vec{C}_T \tag{6}$$

where subscript S means satellite and subscript T means target. Time 0 is selected to be the instant when a given target is in the middle of the azimuth illumination time. Taking the square of both sides in (1) and using the relation (e.g. [17])

$$\sqrt{1+x} = 1 + \tfrac{1}{2}x - \tfrac{1}{8}x^2 + \tfrac{1}{16}x^3 - \tfrac{5}{128}x^4 + \cdots \tag{7}$$

the relative distance as a function of azimuth time can be approximated

$$R_r(t_a) = \sqrt{|\vec{R}(t_a)|^2} = R(1 + \tfrac{1}{2}x - \tfrac{1}{8}x^2 + \tfrac{1}{16}x^3 - \tfrac{5}{128}x^4) \tag{8}$$

where $R = |\vec{R}|$ is the Euclidean norm of the vector in (2). x is defined by

$$x = x_1 t_a + x_2 t_a^2 + x_3 t_a^3 + x_4 t_a^4. \tag{9}$$

It can be shown that

$$x_1 = \frac{2\vec{V}\cdot\vec{R}}{R^2} \tag{10}$$

$$x_2 = \frac{\vec{R}\cdot\vec{A} + \vec{V}\cdot\vec{V}}{R^2} \tag{11}$$

$$x_3 = \frac{\vec{A}\cdot\vec{V} + \frac{1}{3}\vec{R}\cdot\vec{B}}{R^2} \tag{12}$$

$$x_4 = \frac{\frac{1}{3}\vec{V}\cdot\vec{B} + \frac{1}{12}\vec{R}\cdot\vec{C} + \frac{1}{4}\vec{A}\cdot\vec{A}}{R^2}. \tag{13}$$

Using (8), the azimuth phase history is defined as

$$\Phi_a(t_a) = -\frac{4\pi}{\lambda}R_r(t_a) \tag{14}$$

where λ is the radar wavelength. Using (8) the range migration is written

$$R(t_a) = R_r(t_a) - R_r(0) = c_1 t_a + c_2 t_a^2 + c_3 t_a^3 + c_4 t_a^4. \tag{15}$$

The azimuth Doppler frequency is defined by using (14)

$$f(t_a) = \frac{1}{2\pi}\frac{d\Phi_a(t_a)}{dt_a}. \tag{16}$$

Using (8), (14), (15), and (16) it can be shown that

$$f(t_a) \cong a_1 + a_2 t_a + a_3 t_a^2 + a_4 t_a^3 \tag{17}$$

where the c-coefficients in (15) are related to the a-coefficients in (17) by

$$\begin{aligned} c_1 &= -\frac{\lambda}{2}a_1, \qquad c_2 = -\frac{\lambda}{4}a_2, \\ c_3 &= -\frac{\lambda}{6}a_3, \qquad c_4 = -\frac{\lambda}{8}a_4. \end{aligned} \tag{18}$$

The a-coefficients in (17) which we call the Doppler parameters are now defined. It should be noted that all Doppler parameters can be considered as functions of slant range (see Table II). The first Doppler parameter is given by

$$a_1 = -\frac{R}{\lambda}x_1 = -\frac{2\vec{V}\cdot\vec{R}}{\lambda R}. \tag{19}$$

The second Doppler parameter is

$$a_2 = -\frac{2}{\lambda}R(x_2 - \tfrac{1}{4}x_1^2) \tag{20}$$

or using (10) and (11)

$$a_2 = -2\frac{(\vec{R}\cdot\vec{A} + \vec{V}^2)}{\lambda R} + 2\frac{(\vec{V}\cdot\vec{R})^2}{\lambda R^3}. \tag{21}$$

The third and fourth Doppler parameters are given by

$$a_3 = -\frac{3}{\lambda}R\left(x_3 - \frac{x_1 x_2}{2} - \frac{1}{8}x_1^3\right) \tag{22}$$

$$a_4 = -\frac{2}{\lambda}R(2x_4 - x_1 x_3 - \tfrac{1}{2}x_2^2 + \tfrac{3}{4}x2_1 x_2 - \tfrac{5}{32}x_1^4). \tag{23}$$

The first Doppler parameter is usually called the *Doppler centroid* since it is the Doppler frequency in the center of the azimuth beam pattern. The second Doppler parameter is usually called the *azimuth Doppler rate*. The expressions for the Doppler centroid and the azimuth Doppler rate have previously been published in e.g. [10, 16, 18], however, the second term of (21) was not included in [10, 16]. For ERS-1 in yaw steering mode, the second term of (21) is

TABLE I
Orbit Characteristics for Selected Orbit

Semimajor axis (m)	6867000.0
Inclination (^{0})	98.0
Eccentricity	0.001
Argument of perigee (^{0})	90.0
Altitude at ascending node (m)	498841.9
Altitude at perigeum (m)	506044.5

very small. However, for systems which are not yaw steered like RADARSAT and the ERS-1 in roll tilt mode the second term should be included. For narrow-beam systems the second-order coefficient is sufficient for high quality processing (see e.g. [18]). For SAR systems with long integration time the third Doppler parameter and the fourth Doppler parameter must be included as we see in Section IV.

The algorithm described in [19, sect. 3] has been implemented to estimate the Doppler centroid assuming the ERS-1 yaw steering law. The attitude reference system which is fixed to the satellite body (see Fig. 1) is steered to keep the Doppler centroid within one pulse repetition frequency (PRF) band. A pointing vector (parallel to ST) in this system with a look angle a can be calculated. Then this pointing vector is transformed to the inertial reference system. Given the position vector of the satellite $\vec{R}_S$, the position of the target $\vec{R}_T$ is calculated in the inertial reference system by finding the intersection of the pointing vector with the Earth's surface. The Earth's surface is modeled as an ellipsoid. In [19] it is shown how the Doppler centroid given by (19) is estimated. The other Doppler parameters are then estimated using (21)–(23). The Doppler parameters and also the slant range R are estimated as a function of look angle (the look angles used must span the desired swath approximately). Then, the Doppler parameters to be used in the compression filters for a given slant range (given range sample number) are calculated by interpolation of the Doppler parameters. It should be noted that the dot products in the Doppler parameters in (19), (21)–(23) also are dependent on the range parameter R, e.g., $\vec{R}\cdot\vec{A}+\vec{V}\cdot\vec{V}$ is a function of the range to the target.

B. Estimation of Doppler Parameters Using Orbital State Vectors

For the simulation in this work we use orbital state vectors predicted with an orbital propagator based on the theory in [21] given a set of Kepler elements (Table I). The definition of the Kepler elements can be found in [22, pp. 101–102]. If we assume that the orbital state vectors have been predicted and that the position and velocity vectors of the target have been estimated with short time intervals, the coefficients of the time dependent position vector in (1) can be estimated as shown below. We may also mention that the velocity vector of the target can be calculated with the cross-product, $\vec{V}_T=\vec{\omega}_E x\vec{R}_T$, where $\vec{\omega}_E$ is the angular rotation vector of the Earth. Now, the relative velocity vector is defined by differentiating (1)

$$\vec{V}(t_a)=\vec{R}'(t_a). \tag{24}$$

Differentiation of (1) four times, evaluation at $t_a=0$ and using (24) yields

$$\vec{A}=\vec{V}'(0),\qquad \vec{B}=\vec{V}''(0),\qquad \vec{C}=\vec{V}'''(0). \tag{25}$$

Assume that the relative velocity vectors have been estimated at 5 points t_{-2}, t_{-1}, $t_a=0$, t_1, t_2 with spacing Δt_a

$$\vec{V}(t_{-2}),\vec{V}(t_{-1}),\vec{V}(0),\vec{V}(t_1),\vec{V}(t_2). \tag{26}$$

Then the coefficients vectors in (1) or (25) can be estimated by the following approximations (see e.g. [23, pp. 104] for the one-dimensional case)

$$\vec{A}=\frac{\vec{V}(t_1)-\vec{V}(t_{-1})}{\Delta t_a} \tag{27}$$

$$\vec{B}=\frac{(\vec{V}(t_1)-2\vec{V}(0)+\vec{V}(t_{-1}))}{\Delta t_a^2} \tag{28}$$

$$\vec{C}=-\frac{1}{\Delta t_a^3}[\vec{V}(t_1)-\vec{V}(t_{-1})]+\frac{1}{2\Delta t_a^3}[\vec{V}(t_2)-\vec{V}(t_{-2})]. \tag{29}$$

The approximations in (27)–(29) are precise due to the smooth behavior of the relative satellite-target motion over small time intervals (a few seconds). Having obtained estimates for the vectors in (27)–(29), the Doppler parameters in (19), (21)–(23) can be estimated. However it is well known that the Doppler centroid (first Doppler parameter) is better estimated from SAR echo data when available due to its sensitivity to attitude variations. We also see from (19) and (21) that the azimuth Doppler rate is dependent on the Doppler centroid, so the azimuth Doppler rate will be estimated more accurately by estimating the second term in (21) from azimuth

TABLE II
Doppler Parameters at Latitude 49.5° N for X-Band and Yaw Steering

Look angle (^{0})	Range (m)	a_1 (s^{-1})	a_2 (s^{-2})	a_3 (s^{-3})	a_4 (s^{-4})
30.0	588345.7	–640.19	–5937.41	0.1833	0.4684
30.3	590334.7	–638.09	–5916.91	0.1819	0.4637

TABLE III
Doppler Parameters at Latitude 49.4° N for X-Band and No Yaw Steering

Look angle (^{0})	Range (m)	a_1 (s^{-1})	a_2 (s^{-2})	a_3 (s^{-3})	a_4 (s^{-4})
30.0	588345.3	–10988.9	–5934.24	2.6345	0.4670
30.3	590334.3	–11080.5	–5913.70	2.6384	0.4622

spectra and the first term by geometric methods described in [19]. The Doppler parameters are dependent on the definition of the attitude reference system. We simulate here the parameters for both yaw steering and no yaw steering. In [19] is shown how we simulated Doppler parameters for a yaw steered attitude reference system like ERS-1.

The requirements on orbital accuracy are important to analyze to find out whether the EETF4 can be used in practice. In [10] (Section IIIA) the requirements for the orbital accuracy are analyzed for SEASAT by using the fact that different looks are misregistrated using an erroneous azimuth Doppler rate. Using this analysis on the example discussed later in Section IVB with a 5-look X-band SAR (Fig. 6), it can be shown that the azimuth Doppler rate has to be less than 0.065 Hz/s for a misregistration of the first and fifth look of 1/3 m (roughly 1/3 of a pixel). This corresponds to an accuracy of the speed of the satellite of 41 mm/s. If 1/8 m is required the speed has to be determined with an accuracy of 15.4 mm/s. Fast delivery processing of predicted ERS-1 orbit data guarantees accuracy of the radial position less than 28.5 m (3σ) and the accuracy of the along track speed roughly 1/1000 (by rule of thumb among orbit determination experts), which means about 28 mm/s. The precision is degraded at lower altitudes, hence, if real time processing using predicted orbits were required, the tracking had to be improved using appropriate Global Positioning System (GPS) systems (more measurements than in existing tracking systems) to cope with the drag problems at lower altitudes. If not real time processing were required, state-of-the-art precise orbit computation, e.g. [20], might overcome the problem of estimating the Doppler parameters.

The Kepler elements and altitudes are given in Table I for the orbit used for simulation of Doppler parameters. We also see from the table that the altitude is approximately 500 km. In Tables II and III are given the Doppler parameters in (19)–(23) for X-band ($\lambda = 0.312$ m) for yaw steering and no yaw steering, respectively. JERS-1 (1992) and RADARSAT (1995) are not yaw steered, but ERS-1 (1991) and ERS-2 (1995) are mechanically yaw steered, while Envisat's ASAR will be electronically yaw steered. If we talk about SAR resolution of about 1 m, yaw steering will be very important to reduce the enormous range walk corresponding to the Doppler centroids in Table III (about 858 m or 2145 pixels if we assume an integration time of 5 s).

III. FOURTH-ORDER EETF ALGORITHM

An expression for the second order two-dimensional ETF including the Doppler centroid and the azimuth Doppler rate has previously been given in [11] without showing the calculations. Here we start with the point target response in the time domain and show how the point target response in the frequency domain (ETF) is calculated up to fourth order. We start with a general Fourier transform calculation and then calculate an analytical expression for the ETF in the fourth-order case.

A. Two-Dimensional Fourier Transform Calculation

The time domain point target response in general form can be written

$$h(t_r,t_a) = \exp\left[j\left(\Phi_a(t_a) + \Phi_r\left(t_r - \frac{2R(t_a)}{c}\right)\right)\right] \tag{30}$$

where t_r is the range time (fast time). The propagated distance of the SAR pulses is ct_r in the pointing direction, ST, of the beam (see Fig. 1). $\Phi_a(t_a)$ is the azimuth phase function given by (14) which can be written in the fourth-order case (using (16) and (17)) in terms of the Doppler parameters

$$\Phi_a(t_a) = 2\pi(a_1 t_a + \tfrac{1}{2}a_2 t_a^2 + \tfrac{1}{3}a_3 t_a^3 + \tfrac{1}{4}a_4 t_a^4) \tag{31}$$

and $\Phi_r(t_r - 2R(t_a)/c)$ is the range phase function which also takes into account the range migration

$R(t_a)$, and c is the speed of light. We have for simplicity omitted the azimuth antenna gain function since it does not affect the phase in the ETF. We have also omitted the phase due to range at zero azimuth time both in the azimuth phase function and in the range phase function since its consequence is only a complex constant in the ETF. The time variable t_a is as defined in Section IIA the azimuth time (slow time). Now, we take the range Fourier transform of (30) defined by

$$\mathcal{F}_r\{h(t_r,t_a)\} = \int h(t_r,t_a)\exp[-j\omega_r t_r]\,dt_r. \tag{32}$$

Using (14) and (15), the Fourier transform property $\mathcal{F}\{x(t-\Delta t)\} = \exp[j\omega\,\Delta t]\mathcal{F}\{x(t)\}$ and omitting complex constants, the range Fourier transform of the point response can then be written

$$\eta(\omega_r,t_a) = \mathcal{F}_r\{\exp[j\Phi_r(t_r)]\} \cdot \exp\left[-j\left(2\left(\frac{2\pi}{\lambda}+\frac{\omega_r}{c}\right)R(t_a)\right)\right]. \tag{33}$$

To obtain the ETF we apply the azimuth Fourier transform to (33) defined by

$$\mathcal{F}_a[\eta(\omega_r,t_a)] = \int \eta(\omega_r,t_a)\exp[-j\omega_a t_a]\,dt_a \tag{34}$$

which yields

$$H(\omega_r,\omega_a) = \mathcal{F}_r\{\exp[j\Phi_r(t_r)]\} \cdot \int \exp\left[j\left(-2\left(\frac{2\pi}{\lambda}+\frac{\omega_r}{c}\right)R(t_a)-\omega_a t_a\right)\right]dt_a. \tag{35}$$

The integral in (35) can be solved by the principle of stationary phase (see (52)–(55)). Then we use the phase function in the integrand of (35)

$$\phi(t_a) = -2R(t_a)\left(\frac{2\pi}{\lambda}+\frac{\omega_r}{c}\right)-\omega_a t_a \tag{36}$$

and find its stationary point t_a^* that satisfies

$$\phi'(t_a^*) = -2R'(t_a^*)\left(\frac{2\pi}{\lambda}+\frac{\omega_r}{c}\right)-\omega_a = 0. \tag{37}$$

Then the ETF can be written

$$H_{\text{ETF}}(\omega_r,\omega_a;R) = \mathcal{F}_r\{\exp[j\Phi_r(t_r)]\}\sqrt{\frac{2\pi}{|\phi''(t_a^*)|}} \cdot \exp\left[j\frac{\pi}{4}\text{sgn}[\phi''(t_a^*)]\right]\exp[j\phi(t_a^*)] \tag{38}$$

where t_a^* is the stationary point of (37) and sgn means the sign of. We have also indicated the dependency of slant range R. It can be seen that t_a^* is range dependent taking a look at (15) and (18). In general, (37) can be solved numerically, e.g. with Newton's method described, e.g. in [23, p. 4]. However, this may require considerable computation since several iterations usually are required. In this work we find an analytical solution and show in Section IIIB how a fourth-order ETF is calculated.

The Fourier transform of the transmitted signal in the first factor in (38) for the specific case of a linear FM chirp is given by (again using the stationary phase approximation)

$$\mathcal{F}_r\left\{\exp\left[-j\frac{1}{2}b_2 t_r^2\right]\right\} = C_r\exp\left[j\frac{\omega_r^2}{2b_2}\right] \tag{39}$$

where b_2 is the range chirp rate and C_r is a complex constant due to the stationary phase approximation. The transmitted range signal of the ETF in (38) (the first factor) can in principle be of arbitrary form, hence this algorithm also can use a general range chirp replica. We processed an ERS-1 SAR image with a second-order EETF [14] with and without replica and observed a degradation in range resolution when the linear FM chirp was used instead of the replica.

B. Calculation of Fourth-Order ETF

Now we calculate the fourth-order ETF (ETF4) for a SAR in orbit around the rotating Earth. Assuming a fourth-order model and using (15), (37) can be written

$$-2\left(\frac{2\pi}{\lambda}+\frac{\omega_r}{c}\right)(c_1+2c_2t_a+3c_3t_a^2+4c_4t_a^3)-\omega_a = 0. \tag{40}$$

The method to solve (40) is discussed in Appendix B. Inserting the solution in (70) into (36) and using (15) and (18) yields

$$\phi(t_a^*) = \lambda\left(a_1t_a^*+\frac{a_2}{2}(t_a^*)^2+\frac{a_3}{3}(t_a^*)^3+\frac{a_4}{4}(t_a^*)^4\right) \cdot\left(\frac{2\pi}{\lambda}+\frac{\omega_r}{c}\right)-\omega_a t_a^*. \tag{41}$$

The fourth-order ETF is then given by inserting (41) into (38)

$$H_{\text{ETF4}}(\omega_r,\omega_a;R) = C_a\mathcal{F}_r\{\exp[j\Phi_r(t_r)]\}\exp[j\phi(t_a^*)] \tag{42}$$

where C_a can very well be approximated to be a constant although it is slightly varying over the variables of interest. To summarize: Given the range dependent Doppler parameters, a_1,a_2,a_3,a_4, in (19) and (21)–(23) the fourth-order ETF can be evaluated for a given pair of frequencies, (ω_r,ω_a), by using (18), (41), (42), (63)–(65), and (70). It may be noted that for a given pair of range and azimuth frequencies (ω_r,ω_a), a solution of a cubic equation has to be evaluated. However, the solution is given explicitly and no iteration is needed. The ETF includes the so-called secondary range compression (SRC) which

is easily shown in the second-order case [11, 14]. For large Doppler centroid variations smaller blocks may be necessary for the EETF, however, this is also the case for the SRC algorithm as mentioned in [24].

C. Calculation of Range Variant Fourth-Order Phase Corrections

If the Doppler parameters were independent of location in a SAR scene, that is space invariant, the same ETF could be used over all of the scene. However, in real SAR data the parameters have to be updated as indicated in Fig. 5. If large blocks are processed with the same filter, phase corrections have to be calculated to account for the errors which have been introduced in the data on both sides of the center of a block. This approach speeds up the ETF algorithm as shown in Sections IIID and IVB, but also takes care of the phase preservation.

We first approximate the q-parameter in (64). We assume that the term ω_r/c is small compared with $2\pi/\lambda$. Then (64) can be approximated

$$\tilde{q} = q_1 + q_2\omega_a \tag{43}$$

where

$$q_1 = \frac{c_1}{8c_4} + \frac{1}{64}\left(\frac{c_3}{c_4}\right)^3 - \frac{1}{16}\frac{c_2c_3}{c_4^2} \tag{44}$$

$$q_2 = \frac{\lambda}{32\pi c_4}. \tag{45}$$

We have approximated (64) to be independent of the range frequency. Then (64) can be written

$$\tilde{y}_1(c_1,c_2,c_3,c_4) = \sqrt[3]{-\tilde{q} + \sqrt{\tilde{q}^2 + p^3}} + \sqrt[3]{-\tilde{q} - \sqrt{\tilde{q}^2 + p^3}}. \tag{46}$$

For example, for an S-band system and assuming a range bandwidth of 300 MHz, the term ω_r/c is less than 0.8 percent of the term $2\pi/\lambda$ and less than 0.3 percent for X-band. The stationary point solution is then given by using (70)

$$t_a^* = \tilde{y}_1(c_1,c_2,c_3,c_4) - \frac{c_3}{4c_4}. \tag{47}$$

Likewise, the stationary point solution for a different set of Doppler parameters in a given range distance from the middle of a block is

$$\hat{t}_a^* = \tilde{y}_1(\hat{c}_1,\hat{c}_2,\hat{c}_3,\hat{c}_4) - \frac{\hat{c}_3}{4\hat{c}_4}. \tag{48}$$

We also approximate (41) and having (18) in mind

$$\phi(t_a^*) = -\frac{4\pi}{\lambda}(c_1t_a^* + c_2(t_a^*)^2 + c_3(t_a^*)^3 + c_4(t_a^*)^4) - \omega_a t_a^*. \tag{49}$$

Then the phase correction in a given range distance from the middle of a range compressed block is given by the difference of (49) and equation (49) calculated at the stationary point given by (48)

$$\Delta\phi_{\text{EETF4}}(\omega_a;R,R_m) = \phi(t_a^*;R_m) - \phi(\hat{t}_a^*;R) \tag{50}$$

where we also indicate the range dependency. Since the phase function in (49) is range dependent, (50) must be estimated for each range position R around the block center R_m of a range compressed block. The fourth-order ETF together with the phase corrections in (50) we call the fourth-order EETF or simply EETF4. The phase corrections in (50) are multiplied with the range compressed data prior to inverse azimuth fast Fourier transform (FFT) (see Fig. 5). To evaluate (50), equations (43)–(49) have to be used.

D. Implementation

The flow diagram of the algorithm is shown in Fig. 5. A block of raw data is two-dimensionally Fourier transformed by using 2D FFTs. Then the two-dimensional filter, which is the complex conjugate of the fourth-order ETF given in (42), is multiplied by the Fourier transformed raw data. Then an inverse range FFT is applied and then the phase corrections given by (50) are multiplied by the data. It should be noted that the effect of (50) is to perform the azimuth compression perfectly for all azimuth lines within the block. Furthermore, neighboring range blocks are concatenated perfectly and the phase preservation is taken care of. Due to these phase corrections many azimuth lines can be processed from each block which makes the algorithm fast (see example in IVB). The final step is an inverse azimuth FFT. The flow diagram in Fig. 5 shows implementation of processing for 1 block of data. The number of samples in the block in range is $N_{\text{ra}} = 2048$ and in azimuth $N_{\text{az}} = 8192$.

IV. SIMULATION EXAMPLES

A. Analysis of Azimuth Compression

We show here that a fourth-order ETF may be necessary to achieve high image quality and that a second-order ETF becomes inadequate for processing SAR images with resolution around 1 m and several looks. The azimuth filter is dependent on all Doppler parameters, so an analysis of the azimuth impulse response shows us which Doppler parameters are necessary to satisfy a given image quality. The behavior of the impulse response is analyzed with a quite high PRF (50 kHz) in order to get many samples in the mainlobe and in one sidelobe.

We use a one-dimensional ETF with zero range frequency in (38), $H_{\text{ETF}n}(0,\omega_a)$, where ETF$n$ means ETFn of order n. The azimuth phase history,

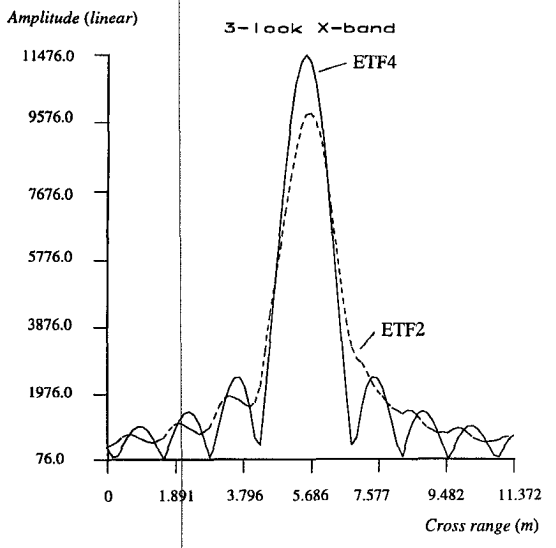

Fig. 2. 3-look azimuth X-band signal for yaw steering compressed with ETF4 (solid) and ETF2 (long-dashed). Integration time for each look is 0.9 s.

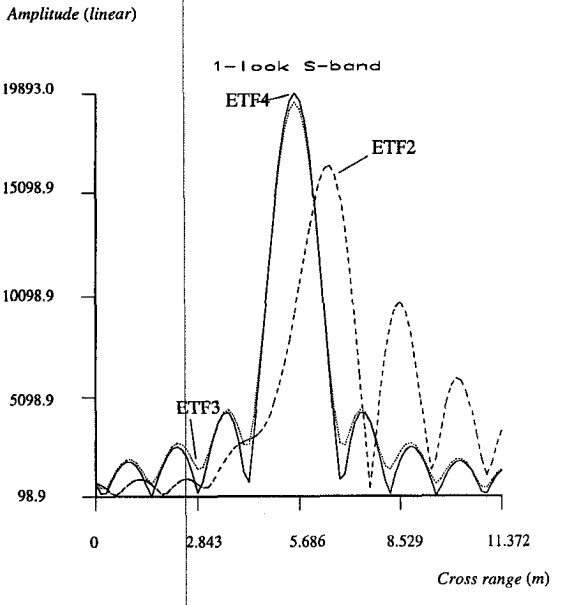

Fig. 3. 1-look azimuth S-band signal for no yaw steering compressed with ETF4 (solid), ETF3 (short-dashed) and ETF2 (long-dashed). Integration time is 2.7 s.

$\Phi_{\text{Kepler}}(t_a)$, is generated by simulation of a Kepler orbit using an orbit propagator based on the theory in [21]. Now, let the Fourier transform of the Kepler azimuth signal be $X_{\text{Kepler}}(\omega_a)$. Then the azimuth compressed signal is given by

$$x_{\text{Kepler}}(t_a) = \mathcal{F}_a^{-1}\{X_{\text{Kepler}}(\omega_a) \cdot H^*_{\text{ETF}n}(0,\omega_a)\}. \tag{51}$$

In Fig. 2 the compressed azimuth signals (no window weighting) is plotted using second-order ETF (ETF2) and fourth-order ETF (ETF4). The Doppler parameters in Table II were used, which correspond to yaw steering. For the ETF2 curve we simulated a second-order ETF by letting $a_3 = 0$ and

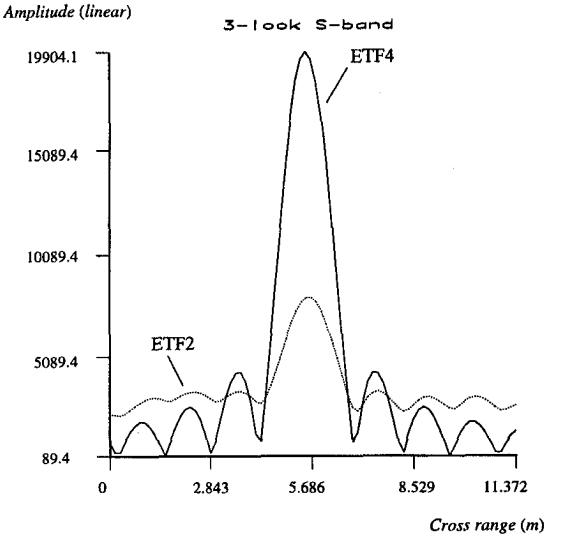

Fig. 4. 3-look azimuth S-band signal for yaw steering compressed with ETF4 (solid) and ETF2 (short-dashed). Integration time for each look is 2.7 s.

a_4 be small. (a_4 cannot be 0, see (70)). For 1-look X-band ($\lambda = 0.032$ m) the curves for ETF4 and ETF2 (not shown) are practically equal, however, for 3 looks the degradation is substantial for ETF2. It is obvious that a second-order ETF is not sufficient to give a satisfactory 3-look point target response. The peak intensity loss if 1.33 dB and the resolution broadening is 12.8 percent. The azimuth resolution is 1.17 m when look integration time is 0.9 s. The sidelobes are also smeared.

In Fig. 3 are shown 1-look responses for ETF2, ETF3, and ETF4 for S-band ($\lambda = 0.094$ m) with no yaw steering. Note that the integration time for an S-band SAR is three times that of an X-band SAR at the same resolution. Even for 1-look there is a small degradation when the fourth Doppler parameter is omitted (ETF3). The degradation is quite large using the ETF2 algorithm. This is due to the third Doppler parameter which is much larger than for yaw steering (compare Tables II and III). We see that the sidelobes are quite asymmetrical and the response is skewed. The response of ETF2 in Fig. 2 is also weakly skewed due to a significant value of the third Doppler parameter for yaw steering.

In Fig. 4 the 3-look responses are shown for S-band for a yaw steered SAR. The ETF2 curve is degraded and unacceptable in comparison with the ETF4 response. Note that the look bandwidth is the same for Figs. 3 and 4, hence, the total bandwidth is three times larger in Fig. 4 than in Fig. 3. The degradation of the ETF2 response in Fig. 4 would be even worse if the SAR were not yaw steered.

B. Simulated Point Target Responses

In order to test the 2-D fourth-order EETF we simulated raw data point targets with the parameters

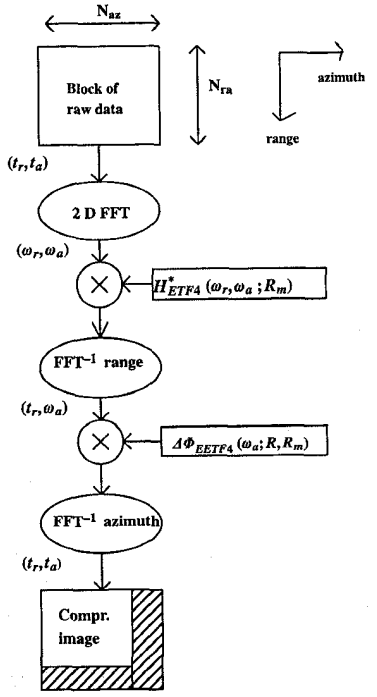

Fig. 5. Flow diagram for EETF algorithm. Shaded regions in compressed image correspond to wasted data due to size of two-dimensional filter.

given in Table IV. Due to memory limitations only the raw data of one look were simulated and processed with EETF4. Different processed looks were written to file and added incoherently when all looks had been processed. It was possible to run the EETF4 algorithm with two matrices of size 2048×8192 complex samples in single precision on an HP9000 computer. The algorithm needed about 280 MBytes of virtual memory.

In Fig. 6 are shown one half of two blocks with nine 5-look point target responses (X-band). The block boundary between the range blocks is indicated in the figure, where one of the point targets is located.

TABLE IV
Sar Simulation Parameters

RF–center frequency	9.6 GHz
Range chirp bandwidth	300 MHz
Range chirp duration	1.25 μs
Sampling frequency	370 MHz
Integration time per look	1.02 s
Pulse repetition frequency	7500 Hz

One point target is located in the middle of each of the blocks. The calculated range resolution is 0.92 m and the aximuth resolution is 1.17 m with window function $W(\omega) = 0.7 + 0.3\cos(\omega/B_p)$, where B_p is the processed bandwidth and ω the angular frequency in either azimuth or range. With this window function, the calculated azimuth resolution is 1.24 pixels and the range resolution 1.23 pixels. In Table V the most usual image quality attributes for point responses are given for each of the looks and for the 5-look image (average of all looks). The quality attributes are estimated as average of the 9 point targets in Fig. 6. We see that the measured azimuth resolution for the 5-look image is 1.22 pixels which is very close to the calculated value of 1.24 pixels. The corresponding values for the range resolution are 1.30 and 1.23. Since the algorithm does not vary the range cell migration correction within one block, the slightly increased range resolution may be the consequence. Peak amplitudes are estimated as the ratio of maximum and minimum amplitude of the 9 point targets for each of the looks (1–5) and for all looks averaged (5-look). We also see that peak amplitudes of the responses of the outer looks (look 1 or look 5) are below the peak amplitude of the center look (look 3), but only 0.038 dB. The peak variation is larger for the outer looks than for the center look. We see that for look 5 the peak

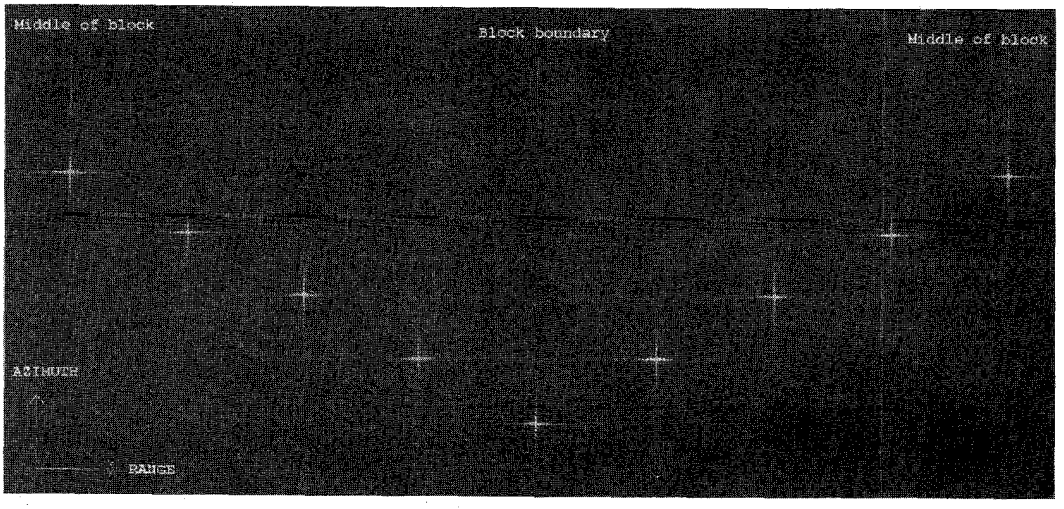

Fig. 6. 5-look point target responses for X-band processed with fourth-order EETF. Azimuth and range resolution approximately 1 m.

TABLE V
Measured Image Quality Attributes

	Look 1	Look 2	Look 3	Look 4	Look 5	5–look (sum)
Az. res. (pixels)	1.226	1.219	1.217	1.220	1.227	1.221
3 stdev az. res (pixels)	0.004	0.004	0.002	0.003	0.004	0.004
Ra. res (pixels)	1.297	1.301	1.303	1.300	1.297	1.300
3 stdev ra. res (pixels)	0.121	0.034	0.003	0.050	0.140	0.074
ISLR (dB)	−15.638	−15.738	−15.714	−15.754	−15.703	−15.809
3 stdev ISLR (dB)	0.424	0.231	0.206	0.217	0.357	0.211
Peak amplitude	22878.8	22937.8	22962.7	22927.9	22862.9	22882.7
Peak variation (dB)	0.213	0.066	0.009	0.009	0.249	0.123

Note: The azimuth resolution (az.res.), range resolution (ra.res), integraded side lobe level ratio (ISLR) and peak amplitude are averaged over 9 point targets. Three standard deviations (stdev) of the quality attributes are shown. Peak variation is the ratio of maximum and minimum amplitude of the nine point targets.

variation is 0.249 dB. This is slightly above the quality requirements usually set for operational SAR processing. However, the 5-look image has a peak variation close to 0.1 dB which could be accepted. The increasing degradation for the outer looks is probably due to the approximation of (64) yielding (43). We see from (64) that the approximation is less accurate for higher azimuth frequencies, which may cause the outer looks to be more degraded than the center look. The EETF4 also assumes that the range migration does not vary over a block in range direction. This may also cause a loss in intensity for the outer looks. The peak variation for a 3-look image is well below 0.1 dB. The measured integrated sidelobe level ratio (ISLR) figures in Table V are well below the requirements usually set at ground stations.

The size of the FFT in range direction was 2048 points when the 5-look image was processed. The output number of pixels was 1100 pixels (in range) from each block to take into account range migration which is 486 samples for look 5. The range chirp was 462 so the number of output pixels is $2048 - 462 - 486 = 1100$. This is considered to be quite efficient processing. As a comparison, for operational ERS-1 processing on the ground stations the number of output samples is around 1300 for a 2048-point FFT. The width of the swath defined in Table II might be quite realistic for a SAR with long integration time, so the swath could be processed with 4 blocks in range. From the analysis above we can conclude that a block size up to 1100 azimuth lines (using 2048-point range FFT) can be processed for a 5-look X-band SAR with 1 m resolution. From the above analysis we see that the number of output azimuth lines is a large fraction of the FFT size, hence, the algorithm is efficient and thus fast.

A quantative error analysis on the phase preservation is usually performed by processing two images from the same real raw data with different starting points in azimuth and range, and then taking the difference of the overlapping regions [27]. A measure for the goodness of phase preservation is the mean of this phase difference and its standard deviation. Of course, there exist no real raw data for the kind of SAR analyzed, however, simulation of raw data from existing SAR images could be done. We don't assess the phase preservation properties of the EETF4, however, we tested the phase preservation in real ERS-1 data using the EETF2 algorithm which is designed in the same way as EETF4. With offset 100 pixels in range and azimuth we achieved mean less than 0.001°, standard deviation 2.4° and no discontinuities between different blocks. As a comparison (although the offset was not specified) in [27] a standard deviation of 7° was achieved using the range-Doppler algorithm. We expect that the EETF4 algorithm also is phase preserving with high quality.

V. CONCLUSIONS

A new fast algorithm, called EETF4 tailored for spaceborne SAR processing, has been developed, implemented, and tested. It was tested for a realistic case with respect to orbit geometry, swath width and SAR parameters. The need for fourth-order azimuth phase history has been demonstrated for 3-look X-band and 1-look S-band at approximately 1 m resolution. It has been shown that the EETF4 algorithm may be used to process point target responses for a 5-look X-band SAR with a quality satisfying the requirements usually set for operational processing. The algorithm is expected to have good phase preservation properties.

APPENDIX A. STATIONARY PHASE APPROXIMATION

The principle of stationary phase can be found in e.g. [25, p. 744–751] where it was applied in optics. Here we review very briefly the principle as described in [26, pp. 142–146]. We want to find the spectrum of

a signal $s(t)$ on the form

$$s(t) = a(t)\exp[jf(t)] \tag{52}$$

where t is the time variable, $a(t)$ is the complex envelope and $f(t)$ is the phase of the signal. Then we have to solve the Fourier transform

$$S(\omega) = \int_{\infty}^{\infty} a(t)\exp[-j(\omega t - f(t))]\,dt \tag{53}$$

where ω is the angular frequency. To get a more convenient form of the solution of (53) than in [26] we define the phase function in (53) as

$$\phi(t) = -\omega t + f(t). \tag{54}$$

Under the assumption of a sufficient large bandwidth time product of the signal $s(t)$ and a smooth envelope function $a(t)$, the spectrum in (53) can be approximated

$$S(\omega) \cong \sqrt{\frac{2\pi}{|\phi''(t^*)|}}a(t^*)\exp\left[j\left(\phi(t^*) + \frac{\pi}{4}\text{sgn}[\phi''(t^*)]\right)\right] \tag{55}$$

where sgn is the sign function and the stationary point t^* satisfies

$$\phi'(t^*) = 0. \tag{56}$$

APPENDIX B. CALCULATION OF FOURTH-ORDER ETF

To find the solution of third-order equation in (40) we rewrite it on the form

$$\alpha t_a^3 + \beta t_a^2 + \gamma t_a + \delta = 0 \tag{57}$$

where

$$\alpha = 4c_4, \qquad \beta = 3c_3,$$
$$\gamma = 2c_2, \qquad \delta = \frac{\omega_a}{2\left(\frac{2\pi}{\lambda} + \frac{\omega_r}{c}\right)} + c_1. \tag{58}$$

Equation (57) can be solved by defining a new variable y (see e.g. [17]) by

$$t_a = y - \frac{\beta}{3\alpha}. \tag{59}$$

Equation (57) can then be written

$$y^3 + 3py + 2q = 0 \tag{60}$$

where

$$p = -\frac{1}{9}\left(\frac{\beta}{\alpha}\right)^2 + \frac{\gamma}{3\alpha} \tag{61}$$

$$q = \frac{2}{54}\left(\frac{\beta}{\alpha}\right)^3 - \frac{1}{6}\frac{\beta\gamma}{\alpha^2} + \frac{\delta}{2\alpha}. \tag{62}$$

Inserting (58) into (61) and (62) yields

$$p = -\frac{1}{16}\left(\frac{c_3}{c_4}\right)^2 + \frac{1}{6}\frac{c_2}{c_4} \tag{63}$$

$$q = \frac{c_1}{8c_4} + \frac{1}{64}\left(\frac{c_3}{c_4}\right)^3 - \frac{1}{16}\frac{c_2c_3}{c_4^2} + \frac{\omega_a}{16c_4\left(\frac{2\pi}{\lambda} + \frac{\omega_r}{c}\right)}. \tag{64}$$

There is one real solution to the equation in (60) if $q^2 + p^3 \geq 0$ and 3 real solutions if $q^2 + p^3 < 0$. The solution in the first case [17] is given by (Kardanische formula)

$$y_1 = \sqrt[3]{-q + \sqrt{q^2 + p^3}} + \sqrt[3]{-q - \sqrt{q^2 + p^3}} \tag{65}$$

and if $q^2 + p^3 < 0$ the 3 solutions are given by

$$y_{-1} = 2\sqrt{-p}\cos\left[\frac{\phi}{3}\right] \tag{66}$$

$$y_{-2} = -2\sqrt{-p}\cos\left[\frac{\phi}{3} + \frac{\pi}{3}\right] \tag{67}$$

$$y_{-3} = -2\sqrt{-p}\cos\left[\frac{\phi}{3} - \frac{\pi}{3}\right] \tag{68}$$

where

$$\cos\phi = \frac{-q}{\sqrt{-p^3}}. \tag{69}$$

The selection of solution in (66)–(68) is simple since the solution must be within the time interval for a given look. It turns out that the two other solutions are far from the time interval corresponding to a given look and are not physically meaningful. Selecting the first solution in (65) as an example and inserting (65) into (59) yields

$$t_a^* = y_1 - \frac{c_3}{4c_4}. \tag{70}$$

ACKNOWLEDGMENT

The author wishes to thank Per Atle Våland and Terje Wahl, both at the Norwegian Defence Research Establishment, for their great enthusiasm for the new algorithm.

REFERENCES

[1] Cumming, I. G., and Bennet, J. R. (1979)
Digital processing of Seasat SAR data.
In *Proceedings of the International Conference on Acoustics and Signal Processing*, Washington, DC, Apr. 2–4, 1979, 45–47.

[2] Jin, M. Y., and Wu, C. (1984)
A SAR correlation algorithm which accommodates large range migration.
IEEE Transactions on Geoscience and Remote Sensing, **GE-22**, 6 (Nov. 1984), 592–597.

[3] Rocca, F. (1987)
Synthetic aperture radar: A new application for wave equation techniques.
SEP-56, 1987, 167–189.

[4] Cafforio, C., Prati, C., and Rocca, F. (1991)
SAR data focusing using seismic migration techniques.
IEEE Transactions on Geoscience and Remote Sensing, **27**, 2 (Mar. 1991), 194–207.

[5] Raney, K. R., and Vachon, P. W. (1989)
A phase preserving SAR processor.
In *Proceedings of IGARSS'89*, Vancouver, Canada, July 10–14, 1989, 2588–2591.

[6] Raney, K. R. (1992)
An exact wide field digital imaging algorithm.
International Journal of Remote Sensing, **13**, 5 (Mar. 1992), 991–998.

[7] Runge, H., and Bamler, R. (1992)
A novel high precision SAR focusing algorithm based on chirp scaling.
In *Proceedings of IGARSS'92*, Houston, TX, May 26–29, 1992, 372–375.

[8] Raney, K., Runge, H., Bamler, R., Cumming, I. G., and Wong, F. H. (1994)
Precision SAR processing using chirp scaling.
IEEE Transactions on Geoscience and Remote Sensing, **32**, 4 (July 1994), 786–799.

[9] Franceschetti, G., Lanari, R., and Marzouk, E. S. (1995)
Efficient and high precision space-variant processing of SAR data.
IEEE Transactions on Aerospace and Electronic Systems, **31**, 1 (Jan. 1995), 227–237.

[10] Li, F. K., Held, D. N., Curlander, J. C., and Wu, C. (1985)
Doppler parameter estimation for spaceborne synthetic-aperture radars.
IEEE Transactions on Geoscience and Remote Sensing, **GE-23**, 1 (Jan. 1985), 47–55.

[11] Chang, C. Y., Jin, M. Y., and Curlander, J. C. (1992)
SAR processing based on the exact two-dimensional transfer function.
In *Proceedings of IGARSS'92*, Houston, TX, May 26–29, 1992, 355–359.

[12] Jin, M. Y., and Chen, M. (1993)
Analysis and simulation for a spotlight-mode aircraft SAR in circular flight path.
In *Proceedings of IGARSS'93*, Tokyo, Japan, Aug. 18–21, 1993, 1777–1780.

[13] Jin, M. Y. (1992)
An exact processing algorithm for wide beam spaceborne SAR data.
Presented at the ISY Conference, ERS-1/JERS-1 Workshop, Tokyo, Nov. 1992.

[14] Eldhuset, K. (1995)
Fast phase preserving processing of spaceborne SAR data.
Technical report FFI/RAPPORT-95/00644, Norwegian Defence Research Establishment, Kjeller, Norway, 1995.

[15] Bamler, R., Breit, H., Steinbrecher, U., and Just, D. (1993)
Algorithms for X-SAR processing.
In *Proceedings of IGARSS'93*, Tokyo, Japan, Aug. 18–21, 1993, 1589–1592.

[16] Madsen, S. N. (1989)
Estimating the Doppler centroid of SAR data.
IEEE Transactions on Aerospace and Electronic Systems, **31**, 2 (Mar. 1989), 134–140.

[17] Rottmann, K. (1960)
Mathematisce Formelsammlung.
Mannheim: Bibliographisches Institut AG, 1960.

[18] Jin, M. Y. (1993)
Prediction of SAR focus performance using ephemeris covariance.
IEEE Transactions on Geoscience and Remote Sensing, **31**, 4 (July 1993), 914–920.

[19] Eldhuset, K. (1996)
Accurate attitude estimation using ERS-1 SAR raw data.
International Journal of Remote Sensing, **17**, 14 (Sept. 1996), 2827–2844.

[20] Andersen, P. H., Aksnes, K., and Hauge, S. (1995)
Precise ERS-1 orbit calculation.
Bulletin Geodesique, **69** (1995), 192–199.

[21] Aksnes, K. (1971)
On the use of the Hill variables in artificial satellite theory: Brouwer's theory.
Astr. J., **17** (1971), 70–75.

[22] Roy, A. E. (1988)
Orbital Motion.
Bristol: Adam Hilger, 1988.

[23] Cheney, W., and Kincaid, D. (1980)
Numerical Mathematics and Computing.
Monterey: Brooks/Cole, 1980.

[24] Chang, C. Y., Jin, M., and Curlander, J. C. (1989)
Squint mode SAR processing algorithms.
In *Proceedings of IGARSS'89*, Vancouver, Canada, July 10–14, 1989, 1702–1706.

[25] Born, M., and Wolf, E. (1959)
Principles of Optics.
New York: Pergamon Press, 1959.

[26] Curlander, J. C., and McDonough, R. N. (1991)
Synthetic Aperture Radar, System and Signal Processing.
New York: Wiley, 1991.

[27] Bamler, R., and Breit, H. (1992)
Experience with ERS-1 SAR signal processing at the German PAF.
In *Proceedings of IGARSS'92*, Houstin, TX, May 26–29, 1992, 1353–1355.

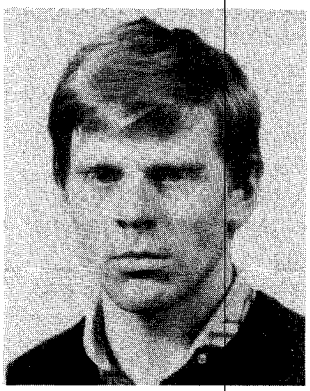

Knut Eldhuset was born in November 1958 and received the cand. scient. (M.Sc.) degree in nuclear physics in 1983 and the dr. scient. (Ph.D.) degree in image processing in 1987. He has been with the Norwegian Defence Research Establishment since 1983 and has worked with satellite orbit simulation, SAR image analysis, SAR processing and image compression techniques. During the years 1985 to 1992 he mainly worked with and developed an automatic demonstration system for ships and ship wakes. He has developed ERS-1 and JERS SAR processing algorithms at Tromsø Satellite Station. During 1993 he performed a study for the European Space Agency on scanSAR processing for Envisat. He has developed a second-order phase preserving SAR processor (extended exact transfer function) which has been industrialized by Kongsberg Spacetec and delivered to the ground stations in Singapore and Tromsø for ERS-2 and RADARSAT processing. From 1990 to 1994 he was a censor in remote sensing at the Norwegian Institute of Technology and from 1994 he has acted as an advisor for Tromsø Satellite Station in SAR processing algorithms for RADARSAT. Since 1996 he has been Principal Investigator of an Announcement of Opportunity ESA project in ERS tandem INSAR processing with applications to DEM generation, glacier and ice motion.